

# Observation of quantum thermalization restricted to Hilbert space fragments

Luheng Zhao,<sup>1</sup> Prithvi Raj Datla,<sup>2</sup> Weikun Tian,<sup>1</sup> Mohammad Mujahid Aliyu,<sup>1</sup> and Huanqian Loh<sup>1,2,3,\*</sup>

<sup>1</sup>Centre for Quantum Technologies, National University of Singapore, 117543 Singapore, Singapore

<sup>2</sup>Department of Physics, National University of Singapore, 117542 Singapore, Singapore

<sup>3</sup>Duke Quantum Center and Department of Electrical and Computer Engineering, Duke University, Durham, NC 27708, USA

Quantum thermalization occurs in a broad class of systems from elementary particles to complex materials. Out-of-equilibrium quantum systems have long been understood to either thermalize or retain memory of their initial states, but not both. Here we achieve the first simultaneous demonstration of thermalization and memory in a quantum system. Using a Rydberg atom array, we observe quantum thermalization restricted to Hilbert space fragments, where the thermalized system retains characteristics of the initial configuration. Intriguingly, states from different subspaces do not thermalize with each other even when they have the same energy. Our work challenges established ideas of quantum thermalization while experimentally resolving the longstanding tension between thermalization and memory. These results may be applied to control entanglement dynamics in quantum processors and quantum sensors.

Quantum thermalization is a central concept for understanding the behavior of systems ranging from atomic nuclei to black holes [1–7]. Quantum thermalization leads to information loss through rapid entanglement spreading, as described by the eigenstate thermalization hypothesis (ETH) that has been postulated to describe the ergodic evolution of isolated quantum systems [8–11]. Conversely, the counterexamples of ETH, notably integrable systems, many-body localization, and quantum many-body scars, are associated with preserving memory of the initial state [12–22]. The question of how thermalization can coexist with memory — two phenomena long considered to be at odds with each other — has generated much debate in the past decade and remains important for finding new ways to control entanglement propagation.

Recently, Hilbert space fragmentation has been put forth as a mechanism through which quantum systems can exhibit rich entanglement dynamics [23–30]. In this mechanism, the Hilbert space is shattered into exponentially many disjointed subspaces, or Krylov subspaces, each of which can be integrable or non-integrable. The fragmentation can originate from approximate conservation laws or imposed kinetic constraints [31–33]. Fragmented systems are important for understanding a host of exotic phenomena including quark confinement, high-temperature superconductivity, and fractional quantum Hall physics [25, 29, 34, 35].

Krylov-restricted thermalization has been conjectured to occur in fragmented systems, by which ETH would be permitted only within a given non-integrable Krylov subspace but be violated with respect to the entire Hilbert space [27, 28]. However, since the Krylov fractures were not thoroughly understood, it was not initially obvious that Krylov-restricted thermalization would occur [23]. The conjecture was later supported by numerics [27], although it was not clear how to translate from theoretical models to an experimental implementation. After all, in physical realizations of fragmented systems, the Hilbert space is often split into energy-conserving blocks [28]. In other words, full thermalization within an energy-conserving subspace would still be con-

sistent with global ETH, which compares a globally entangled state against a thermal ensemble of states *within a narrow energy window* [9]. In fact, for fragmented models derived from kinetic constraints, it is not generally known how the Krylov subspaces would be identified [24]. Even when the Hilbert space fractures are relatively well understood as in dipole-moment-conserving models, a recent experimental study found disagreement between the steady-state observables and theoretical predictions for thermalization within the Krylov fragment, indicating that there is no guarantee for a fragmented system to thermalize within a given subspace [32].

Here we report the first observation of quantum thermalization restricted to Krylov subspaces. The Hilbert space fragmentation in our Rydberg atom array experiment arises from kinetic constraints, which we demonstrate through  $\mathbb{Z}_{2k}$  quantum many-body scarring, generalizing beyond the  $\mathbb{Z}_2$  scarring previously reported in cold-atom setups. We discover Krylov subspaces beyond energy-conserving blocks, which we identify through the configuration of Rydberg atoms (Fig. 1). We observe that while thermalization proceeds in a given subspace, thermalization between energy-degenerate states belonging to different Krylov subspaces is precluded, yielding a clear violation of ETH for the entire Hilbert space. In other words, the thermalized system preserves memory of the initial configuration by storing information through the relevant Krylov subspace.

In our experiment setup, we use a linear chain of equally spaced  $^{87}\text{Rb}$  atoms ( $N = 13 - 19$  atoms) with pseudospin states encoded in their ground  $|g\rangle$  and Rydberg  $|r\rangle$  states ( $\hbar = 1$ ):

$$H = -\Delta \sum_{i=1}^N Q_i + \frac{\Omega}{2} \sum_{i=1}^N X_i + \sum_{j=1}^{N-1} \sum_{i=1}^{N-j} V_{j-1} Q_i Q_{i+j}, \quad (1)$$

where  $i$  indexes the atom,  $V_{j-1} = C_6/(ja)^6$  is the van der Waals interaction between Rydberg atoms,  $a$  is the interatomic spacing,  $\Delta$  is the detuning,  $\Omega$  is the Rabi frequency,  $Q_i = |r_i\rangle \langle r_i|$  is the projector onto the Rydberg state, and  $X_i = |g_i\rangle \langle r_i| + |r_i\rangle \langle g_i|$ . In the  $\{|g\rangle, |r\rangle\}$  basis,  $Z|g\rangle = -|g\rangle$ , and  $Z|r\rangle = +|r\rangle$ . We prepare the initial state through single-site addressing [36] of a subset of the chain, followed by a global

\* huanqian.loh@duke.edu

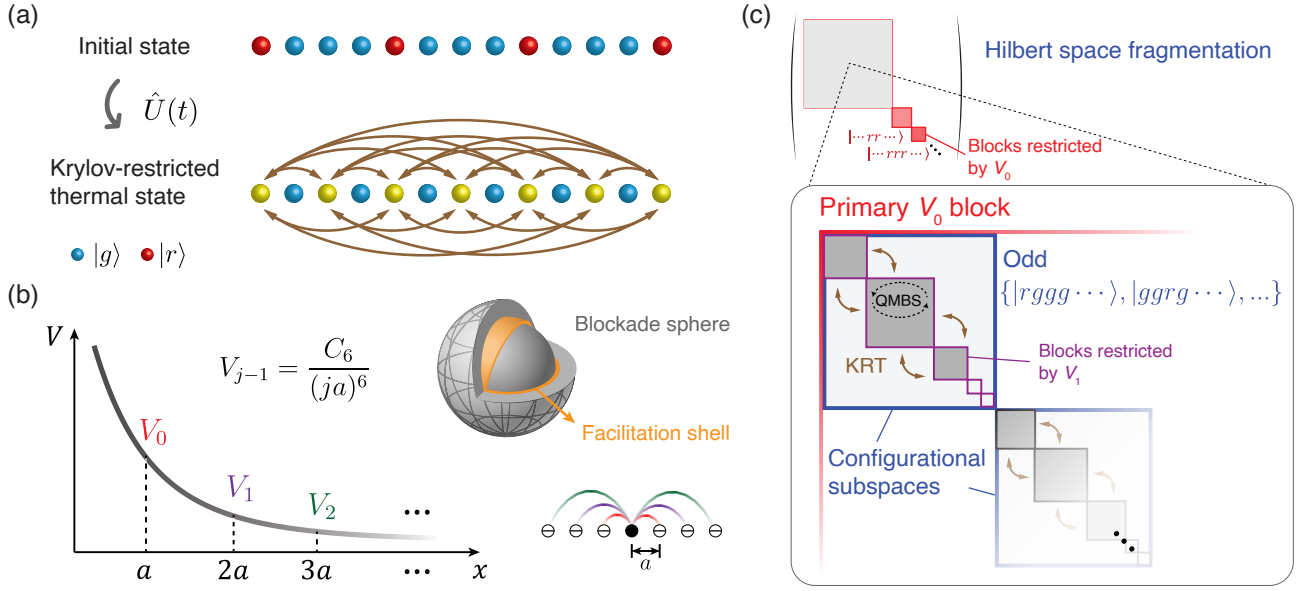


FIG. 1. **Krylov-restricted thermalization arising from Hilbert space fragmentation.** (a) Schematic of a Rydberg atom array initialized in the  $\mathbb{Z}_4$  ordered state and evolving into a Krylov-restricted thermal state, where atoms at odd sites thermalize with each other while atoms at even sites remain frozen. (b) The presence of a Rydberg atom can yield a blockade sphere (gray), within which Rydberg excitations are suppressed, or a facilitation shell (orange), at which Rydberg excitations are allowed. Strong kinetic constraints are engineered by facilitating different orders of the Rydberg interaction. (c) The Hilbert space in the product-state basis is first fragmented into blocks restricted by the  $V_0$  interaction (red), where states in the primary (secondary)  $V_0$  block have zero (one)  $V_0$  energy term, and so on. Within each  $V_0$  block, the Hilbert space is further fragmented into configurational subspaces (blue), e.g. the odd configurational subspace, where Rydberg excitations solely occur on odd-numbered sites of the atom chain. Within each configurational subspace, the Hilbert space is then fragmented into blocks restricted by the  $V_1$  interaction (purple). The finer block structure iterates for higher-order interactions. Krylov-restricted thermalization (KRT) is achieved by lifting the  $V_1$  restriction while maintaining the disconnectivity between configurational subspaces (brown arrows).

$\pi$  pulse for Rydberg excitation. We then turn off the single-site addressing beams and probe the subsequent dynamics by measuring the Rydberg and ground state densities after a given time evolution.

Such a Rydberg atom array quantum simulator is often used in the Rydberg blockade regime, where the presence of a Rydberg atom prevents all other atoms within a blockade radius  $R_b$  from being excited to the Rydberg state, regardless of their precise position within  $R_b$ . In particular, where the blockade radius only covers nearest neighbors such that  $V_0 \gg \Omega \gg V_1$ , dynamics on the chain are constrained such that an atom is allowed to flip its state only if all its immediate neighbors are in the ground state. Such constrained dynamics are captured by an effective PXP model, which has been used to explain quantum many-body scars of  $\mathbb{Z}_2$  order (e.g. revivals between  $|rgrgrg \dots\rangle$  and  $|grgrgr \dots\rangle$ ) [22].

In contrast, here we impose kinetic constraints using facilitation, which means that a Rydberg atom must be present to drive other nearby atoms to the Rydberg state. Applying a global detuning facilitates Rydberg excitations, which lie on a shell of tunable radius given by  $R_f = (C_6/\Delta)^{1/6}$  (Fig. 1b) [37, 38]. We use facilitation to selectively make beyond-nearest-neighbor interactions resonant. Combining facilitation with Rydberg blockade then allows us to achieve a broad class of locally constrained models.

To explain how Krylov subspaces emerge in our system,

we first consider only facilitating nearest-neighbor interactions. Setting the global detuning to  $\Delta = 2V_0$ , we now allow an atom to flip its state only when facilitated by two nearest neighbor Rydberg atoms. This constraint is captured by the effective Hamiltonian given by the QXQ model  $H_{\text{QXQ}} = \frac{\Omega}{2} \sum_i Q_{i-1} X_i Q_{i+1}$ .

At first glance, it appears that the QXQ model can be mapped exactly onto the PXP model by interchanging  $|g\rangle \leftrightarrow |r\rangle$  [30]. Indeed, we observe quantum many-body scars in both the QXQ and PXP models when a subset of the atom array is initialized in the  $\mathbb{Z}_2$  ordered state (Fig. 2a, b). However, while the PXP and QXQ models are symmetrically mapped to each other, the Hilbert space connectivity for experimentally accessible states is different for the two models. When the  $\mathbb{Z}_2$  ordered subarray is surrounded by ground state atoms, the entire system takes part in the scarring dynamics under the PXP model. In contrast, for the QXQ model, the Rydberg atoms at the boundaries of the ordered state and atoms beyond the boundaries remain frozen. The frozen behavior occurs because these atoms do not fulfill the condition of having two adjacent Rydberg atoms as required by the QXQ model. In general,  $|gg\rangle$  substrings, which can be easily prepared, would remain frozen within an atom chain under the QXQ model. In contrast, their symmetric mapping as frozen  $|rr\rangle$  substrings in the PXP model would be experimentally challenging to prepare. As a result, the experimentally accessible subspace is

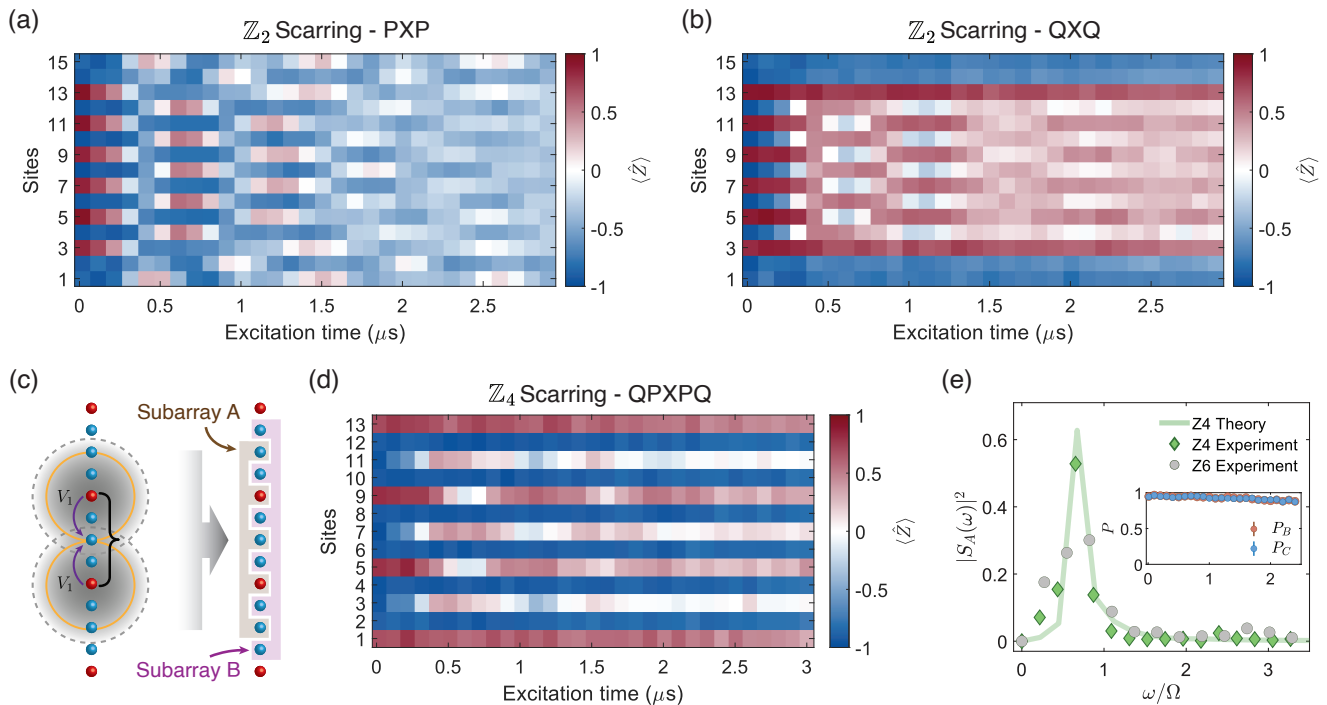


FIG. 2. **Quantum many-body scarring in locally constrained models.** Single-atom-resolved  $Z$  measurements of spin chains in the (a) PXP and (b) QXQ models initialized in  $\mathbb{Z}_2$  ordered states surrounded by ground state atoms. (c) The QPXPQ model is achieved by setting  $\Delta = 2V_1$  with  $V_0, V_1 \gg \Omega$ , such that an atom flips its spin only when flanked by nearest-neighbor ground state atoms and next-nearest-neighbor Rydberg excitations. Under the QPXPQ Hamiltonian, the dynamics of atoms in subarray  $A$  (odd sites, boundary atoms excluded) are distinct from that in subarray  $B$  (even sites). (d) Single-atom-resolved  $Z$  measurements of the spin chain showing the  $\mathbb{Z}_4$  quantum many-body scar at  $\Delta = 2V_1$ . (e) Fourier analysis of the  $\mathbb{Z}_{2k}$  scars observed on subarray  $A$ . Experiment data (green diamonds for  $k = 2$ ) show reasonable agreement with theory (green curve), which predicts a peak at  $\omega \approx 0.67\Omega$ . The experimentally observed  $\mathbb{Z}_6$  scar manifests as a Fourier peak in subarray  $A$  (gray circles) and frozen ground state densities  $P_{B/C}$  in the other two subarrays (inset).

completely connected in the PXP model but fragmented in the QXQ model.

The QXQ model alone, however, is insufficient to effect Krylov-restricted thermalization. This is because the Hilbert space is only fragmented according to energy, so at least one more independent degree of freedom characterizing the subspaces is required to ensure the violation of ETH with respect to energy. To uncover the required degree of freedom, we extend the range of constraints by using successive orders of the van der Waals interaction.

Consider now the regime where only the first two orders of the interaction are large ( $V_0, V_1 \gg \Omega \gg V_2$ ). Setting  $\Delta = 2V_1$  then results in the model:  $H_{\text{QPXPQ}} = \frac{\Omega}{2} \sum_i Q_{i-2} P_{i-1} X_i P_{i+1} Q_{i+2}$ . Explicitly, this means that an atom will only flip its state when its immediate neighbors are ground state atoms and next-nearest neighbors are Rydberg atoms (Fig. 2c). This co-existence of both Rydberg blockade and facilitation constraints gives rise to qualitatively distinct dynamics in different sectors of our system, which we track by partitioning the bulk of the chain into two subarrays  $A$  and  $B$  to highlight their contrasting behavior (Fig. 2c).

Under the QPXPQ model, we observe quantum many-body scars from  $\mathbb{Z}_4$  ordered initial states, with the single-atom-resolved  $Z$  measurements oscillating between two  $\mathbb{Z}_4$  sectors

of the chain, while atoms in the other  $\mathbb{Z}_2$  sector (subarray  $B$ ) remain completely frozen in the ground state (Fig. 2d). The scar oscillations manifest as a single peak in a Fourier analysis of the  $\mathbb{Z}_4$  dynamics (Fig. 2e).

We note that our approach enables us to access a broad class of locally constrained Hamiltonians  $H_{\text{QPXPQ}}(k) = \frac{\Omega}{2} \sum_i Q_{i-k} X_i Q_{i+k} \prod_{j=1}^{k-1} P_{i-j} P_{i+j}$  by setting  $\Delta = 2V_{k-1}$ . Besides  $k = 2$  that corresponds to  $\mathbb{Z}_4$  scarring, we also realize the case of  $k = 3$  by operating in the regime where  $V_1, V_2$ , and  $V_3$  are all large. Here, the bulk of a 19-atom chain is partitioned into three interleaved subarrays ( $A, B, C$ ) and initialized in a  $\mathbb{Z}_6$  ordered state. In this case, we observe quantum many-body scars, as indicated by the Fourier peak in the dynamics between two  $\mathbb{Z}_6$  sectors within subarray  $A$ , whereas the remaining subarrays remain frozen in the ground state (Fig. 2e).

At this point, it is instructive to consider matrix plots of the QPXPQ Hamiltonian in the product state basis. Without loss of generality, we focus on the case of  $k = 2$ . The different interaction energy scales ( $V_0, V_1$ ) fragment the full Hilbert space into blocks containing states of the same energy. As such, it is natural to consider ordering the product-state basis of this chain by their energies with respect to  $V_0$  and  $V_1$  (Fig. 3a). However, the dynamics in Fig. 2d are highly depen-

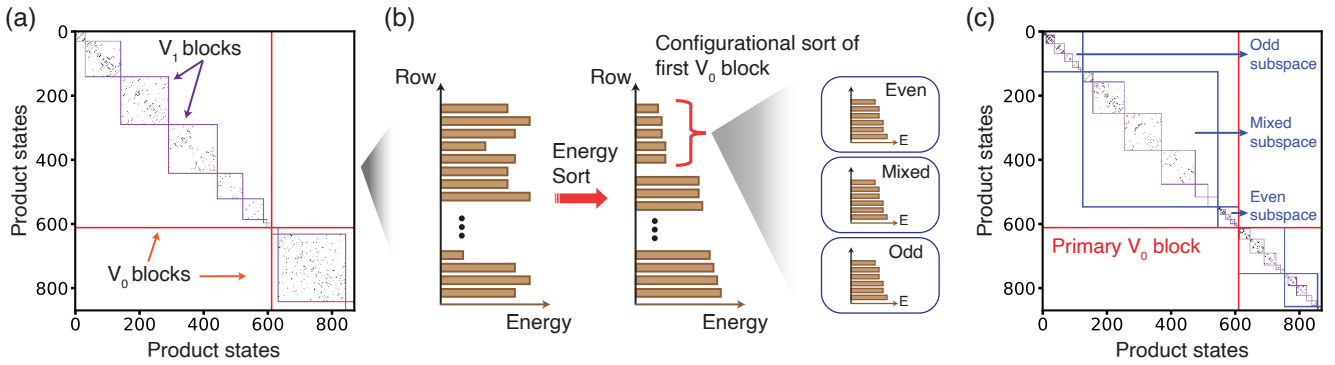


FIG. 3. **Hilbert space fragmentation of a 13-atom open chain.** (a) A zoomed-in matrix plot of the QXPQ Hamiltonian, with the product state basis sorted only by energy. (b) To uncover the Hilbert space fractures, we first sort the product-state basis in energy, from which we identify the first  $V_0$  block. States in each  $V_0$  block are then grouped according to their configuration, after which a final energy sort is performed within each configurational group. (c) The resultant matrix plot, focusing on the first  $V_0$  energy block, after the product-state basis ordering. Disjointed blocks emerge due to different energy scales (red for  $V_0$ , purple for  $V_1$ ) and configurational disconnectivity (blue).

dent on the configuration of the initial state, which suggests the emergence of a Hilbert space structure unrelated to the energy windows.

To capture these observations, we take the product states in the first  $V_0$  block and categorize them according to their configuration. We group product states in the even (odd) subspace if they have Rydberg excitations on only even (odd) sites, and the remaining product states fall in the mixed subspace. This configuration-based sorting gives rise to a secondary block structure as shown in Fig. 3c. Within each configurational subspace, the Hilbert space is further split up according to the  $V_1$  interaction energy scale. While Fig. 3 focuses on the experimentally accessible subspace (i.e. the first  $V_0$  block), the number of fragmented sectors in the entire Hilbert space grows exponentially with the size of the chain. The fact that the odd subspace projects all atoms on even sites into the ground state and remains disconnected from other subspaces under  $H_{\text{QXPQ}}$  allows atoms in subarray  $B$  stay frozen over time.

The disconnectivity between configurational subspaces is no longer present for the blockade-only PPXP Hamiltonian [39], highlighting that facilitation is a necessary ingredient for realizing clean Hilbert space fractures beyond energy considerations in the product-state basis. Intuitively, this arises from the fact that facilitation allows one to selectively excite atoms only at a given distance, whereas Rydberg blockade acts on all atoms within a sphere and therefore lacks such distance selectivity. In other words, Krylov subspaces in our system arise from strong kinetic constraints in the form of conditional excitations from both facilitation and blockade that invoke higher-order interaction terms. Such a fragmented system is distinct from existing proposed models.

Importantly, Fig. 4a predicts that the configurational subspaces remain disconnected upon coupling states that are previously separated in energy by  $V_1$ . We effect the coupling by adding, on top of the first drive at  $\Delta = 2V_1$ , a second drive detuned at  $\Delta' = V_1$ . The two-drive experiments are implemented using Floquet frequency mod-

ulation [40], realizing the effective Hamiltonian [39]:  $H_{\text{KRT}} = \frac{\Omega}{2} \sum_i P_{i-1} X_i P_{i+1} (Q_{i-2} Q_{i+2} + \beta P_{i-2} Q_{i+2} + \beta Q_{i-2} P_{i+2})$ . Here,  $\beta$  is the ratio of Rabi frequencies  $\Omega_{V_1} : \Omega$ .

To contrast the dynamics under  $H_{\text{KRT}}$  versus under  $H_{\text{QXPQ}}$ , we initialize a 13-atom chain in the  $\mathbb{Z}_4$  ordered state, where the atoms are partitioned in the same way as depicted in Fig. 2c. Strikingly, instead of observing generic thermalization across the entire array, we find that the atoms in subarray  $A$  quickly thermalize, whereas atoms in subarray  $B$  remain frozen in the ground state. In fact, introducing the additional  $\Delta' = V_1$  drive couples the boundary atoms to subarray  $A$  and allows them to take part in thermalization, unlike in the QXPQ framework where boundary Rydberg atoms remain frozen and do not take part in scar dynamics. We refer to the collection of atoms in subarray  $A$ , together with the two boundary atoms, as subarray  $A'$ . The restricted-thermalization dynamics can be perceived through a few different measures: comparing the time-dependent staggered magnetization of subarray  $A'$  versus the ground state density for subarray  $B$ , tracking the trajectories of experimentally observed microstate projections, and computing the von Neumann entropy of single atoms in the two subarrays.

Specifically, under  $H_{\text{KRT}}$ , Fig. 4b shows that  $M_{A'}$  quickly decays to the thermal value as predicted by a microcanonical ensemble [39], whereas the ground state density for subarray  $B$  remains high over time. Further, the microstate projections are observed to have a near-uniform spread across the basis of  $(2^{N_{A'}} - 1)$  states (Fig. 4c). This is in stark contrast to the  $\mathbb{Z}_4$  scar behavior, which features persistent revivals in the staggered magnetization  $M_A$  and a periodic trajectory in the constrained product-state basis for the QXPQ model (Fig. 4c). Finally, the average von Neumann entropy  $S_{\text{ent}}$  for atoms in subarray  $A'$  is found to quickly saturate to the thermal value of  $\ln 2$ , whereas it grows much more slowly for atoms in subarray  $B$ . The finite slow decay of  $P_B$  and correspondingly slow growth of  $S_{\text{ent}}^B$  for subarray  $B$  is attributed to deviations from the effective model Hamiltonians [39].

We note that our findings are distinct from previous stud-

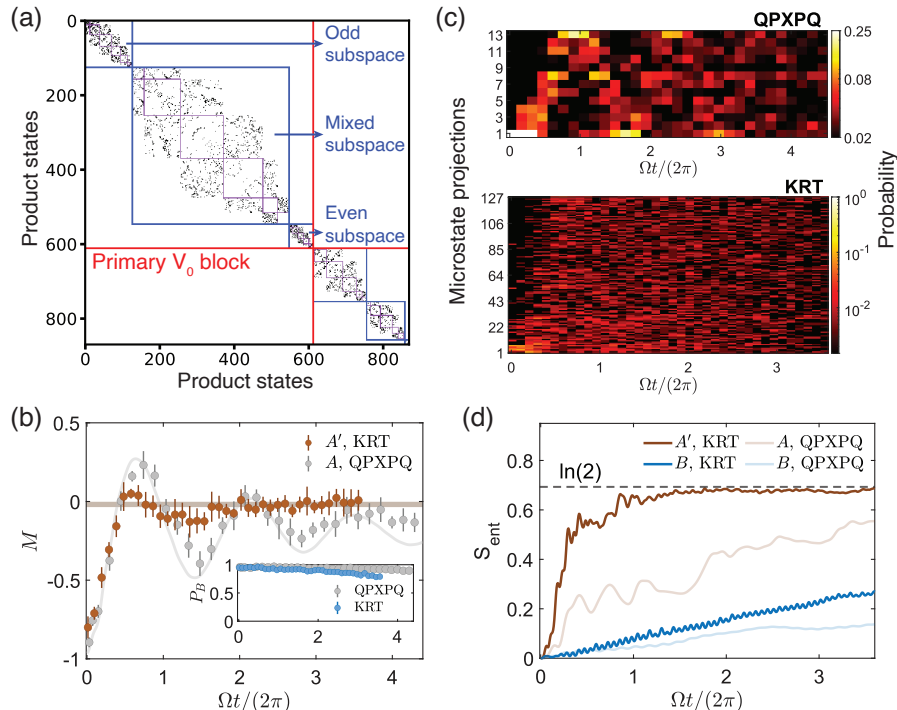


FIG. 4. **Signatures of Krylov-restricted thermalization.** (a) Matrix plot under  $H_{\text{KRT}}$  for a 13-atom linear chain. Relaxing the  $V_1$  energy restriction allows thermalization to proceed within each configurational subspace while the three configurational subspaces remain disconnected. (b) Time-dependent behavior of the staggered magnetization for subarray  $A'$  [39]  $M_{A'}(t) = \frac{1}{N_{A'}} \sum_{i \in A'} (-1)^i \langle Z_i(t) \rangle$  and (inset) ground state density for subarray  $B$ , defined as  $P_B(t) = \frac{1}{N_B} \sum_{i \in B} \langle \hat{P}_i \rangle$ . Under  $H_{\text{KRT}}$ ,  $M_{A'}$  (brown) quickly relaxes from -1 for an initial  $\mathbb{Z}_4$  ordered state to its final thermal value near 0 (horizontal brown line). In contrast, under  $H_{\text{QPXPQ}}$ ,  $M_A$  displays persistent oscillations corresponding to a  $\mathbb{Z}_4$  scar (gray data points with gray theory curve). In both cases, the atoms in subarray  $B$  remain frozen in the ground state. (c) Microstate projections of experimentally measured bitstrings onto the constrained product state basis, ordered by their Hamming distance, under  $H_{\text{QPXPQ}}$  and  $H_{\text{KRT}}$ . (d) Numerical plots of the average von Neumann entropy. For single atoms in subarray  $A'$ ,  $S_{\text{ent}}$  rapidly saturates to the thermal value for subarray  $A'$  under  $H_{\text{KRT}}$  (dark brown).

ies of thermalization with Rydberg atom arrays [22, 41, 42], where states are found to be entangled with all other states within the same energy window [22, 42]. Our observations of strongly site-dependent thermalization, which occurs in the absence of any site-selective addressing, is a manifestation of the configurational disconnectivity due to Hilbert space fragmentation.

Notably, states in the odd configurational subspace never thermalize with any states in the even or mixed configurational subspaces, and vice versa, even when they are *exactly* degenerate in energy (Figs. 4a, 5). This is the smoking-gun signature of Krylov-restricted thermalization, which constitutes a clear violation of the ETH for the full Hilbert space at this energy window, even though we see signatures of thermalization within a given subspace.

We have demonstrated the first realization of Krylov-restricted thermalization, by which we experimentally resolve the longstanding tension between thermalization and memory. Our results prompt a relook at the cornerstone ideas of quantum thermalization [8–11], which may have more stringent requirements beyond energy considerations. Our work can be extended to yield a comprehensive description of Krylov subspaces, which would be important for elucidating the full na-

ture of ETH violation [26, 27, 29]. Our observations open the door to comparisons against other fragmented systems such as dipole-conserving models [23, 24, 32], where Krylov-restricted thermalization can give rise to intriguing fracton dynamics [43]. On the other hand, explorations of non-ergodic dynamics in fragmented systems would provide valuable insights on dynamical phases such as constraint-driven many-body localization (MBL) [44–46] and non-Hermitian skin clusters [47]. Finally, the control of information dynamics in fragmented systems can be expanded through out-of-time-ordered correlators [48, 49] and may be used to enhance quantum information processing and quantum metrology [50].

## ACKNOWLEDGEMENTS

We thank Adam Kaufman, Wen Wei Ho, Ching Hua Lee, and Travis Nicholson for helpful discussions, as well as Fan Jia, Wen Jun Wee, An Qu, and Jiacheng You for technical assistance with the experiment setup. This research is supported by the National Research Foundation, Singapore and A\*STAR under its Quantum Engineering Programme (NRF2021-QEP2-02-P09) and its CQT bridging grant. All

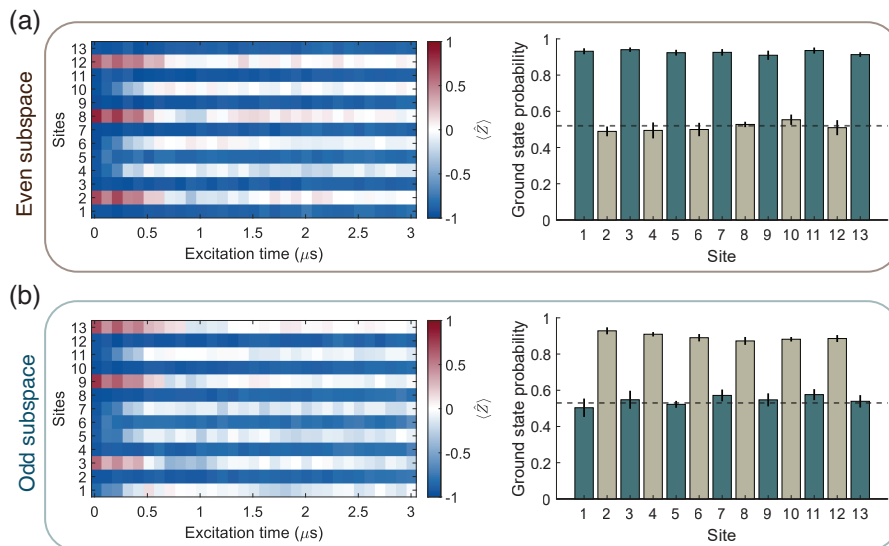


FIG. 5. **Thermalization within distinct subspaces.** (a) Thermalization within the even subspace. Single-atom-resolved dynamics (left) for an array initialized with Rydberg excitations on sites (2, 8, 12). The site-resolved ground state probabilities, time-averaged from  $2.7 \mu\text{s}$  to  $3 \mu\text{s}$  (corresponding to  $\Omega t/(2\pi) = 1.7 - 1.9$ , where  $S_{\text{ent}}$  has already saturated), are shown on the right. Dark (light) green bars indicate the odd (even) subarray. The horizontal dashed line indicates the thermal predicted value. (b) Corresponding dynamics and long-time-averaged ground state probabilities, shown to depict thermalization within the odd subspace. Here the array is initialized with Rydberg excitations on sites (3, 9, 13). Despite the two initial states of (a) and (b) having the same energy, they do not thermalize with each other.

data in this study are available from the corresponding author upon reasonable request.

- 
- [1] V. Zelevinsky, Quantum chaos and complexity in nuclei, *Annual Review of Nuclear and Particle Science* **46**, 237 (1996).
- [2] J. Berges, M. P. Heller, A. Mazeliauskas, and R. Venugopalan, Qcd thermalization: Ab initio approaches and interdisciplinary connections, *Reviews of Modern Physics* **93**, 035003 (2021).
- [3] Z.-Y. Zhou, G.-X. Su, J. C. Halimeh, R. Ott, H. Sun, P. Hauke, B. Yang, Z.-S. Yuan, J. Berges, and J.-W. Pan, Thermalization dynamics of a gauge theory on a quantum simulator, *Science* **377**, 311 (2022).
- [4] S. Rodriguez, J. Feist, M. Verschuuren, F. G. Vidal, and J. G. Rivas, Thermalization and cooling of plasmon-exciton polaritons: towards quantum condensation, *Physical review letters* **111**, 166802 (2013).
- [5] P. Hayden and J. Preskill, Black holes as mirrors: quantum information in random subsystems, *Journal of high energy physics* **2007**, 120 (2007).
- [6] A. Polkovnikov, K. Sengupta, A. Silva, and M. Vengalattore, Colloquium: Nonequilibrium dynamics of closed interacting quantum systems, *Reviews of Modern Physics* **83**, 863 (2011).
- [7] J. Eisert, M. Friesdorf, and C. Gogolin, Quantum many-body systems out of equilibrium, *Nature Physics* **11**, 124 (2015).
- [8] J. M. Deutsch, Quantum statistical mechanics in a closed system, *Physical Review A* **43**, 2046 (1991).
- [9] M. Rigol, V. Dunjko, and M. Olshanii, Thermalization and its mechanism for generic isolated quantum systems, *Nature* **452**, 854 (2008).
- [10] C. Neill, P. Roushan, M. Fang, Y. Chen, M. Kolodrubetz, Z. Chen, A. Megrant, R. Barends, B. Campbell, B. Chiaro, *et al.*, Ergodic dynamics and thermalization in an isolated quantum system, *Nature Physics* **12**, 1037 (2016).
- [11] A. M. Kaufman, M. E. Tai, A. Lukin, M. Rispoli, R. Schittko, P. M. Preiss, and M. Greiner, Quantum thermalization through entanglement in an isolated many-body system, *Science* **353**, 794 (2016).
- [12] T. Kinoshita, T. Wenger, and D. S. Weiss, A quantum Newton's cradle, *Nature* **440**, 900 (2006).
- [13] J. Eisert, M. Cramer, and M. B. Plenio, Colloquium: Area laws for the entanglement entropy, *Rev. Mod. Phys.* **82**, 277 (2010).
- [14] R. Nandkishore and D. A. Huse, Many-body localization and thermalization in quantum statistical mechanics, *Annu. Rev. Condens. Matter Phys.* **6**, 15 (2015).
- [15] M. Schreiber, S. S. Hodgman, P. Bordia, H. P. Lüschen, M. H. Fischer, R. Vosk, E. Altman, U. Schneider, and I. Bloch, Observation of many-body localization of interacting fermions in a quasirandom optical lattice, *Science* **349**, 842 (2015).
- [16] D. A. Abanin, E. Altman, I. Bloch, and M. Serbyn, Colloquium: Many-body localization, thermalization, and entanglement, *Reviews of Modern Physics* **91**, 021001 (2019).
- [17] M. Rispoli, A. Lukin, R. Schittko, S. Kim, M. E. Tai, J. Léonard, and M. Greiner, Quantum critical behaviour at the many-body localization transition, *Nature* **573**, 385 (2019).
- [18] M. Schulz, C. Hooley, R. Moessner, and F. Pollmann, Stark many-body localization, *Physical Review Letters* **122**, 040606 (2019).
- [19] W. Morong, F. Liu, P. Becker, K. Collins, L. Feng, A. Kypriandis, G. Pagano, T. You, A. Gorshkov, and C. Monroe, Observation of Stark many-body localization without disorder, *Nature* **599**, 393 (2021).

- [20] H. Bernien, S. Schwartz, A. Keesling, H. Levine, A. Omran, H. Pichler, S. Choi, A. S. Zibrov, M. Endres, M. Greiner, *et al.*, Probing many-body dynamics on a 51-atom quantum simulator, *Nature* **551**, 579 (2017).
- [21] C. J. Turner, A. A. Michailidis, D. A. Abanin, M. Serbyn, and Z. Papić, Weak ergodicity breaking from quantum many-body scars, *Nature Physics* **14**, 745 (2018).
- [22] D. Bluvstein, A. Omran, H. Levine, A. Keesling, G. Semeghini, S. Ebadi, T. T. Wang, A. A. Michailidis, N. Maskara, W. W. Ho, *et al.*, Controlling quantum many-body dynamics in driven Rydberg atom arrays, *Science* **371**, 1355 (2021).
- [23] P. Sala, T. Rakovszky, R. Verresen, M. Knap, and F. Pollmann, Ergodicity breaking arising from Hilbert space fragmentation in dipole-conserving Hamiltonians, *Physical Review X* **10**, 011047 (2020).
- [24] V. Khemani, M. Hermele, and R. Nandkishore, Localization from Hilbert space shattering: From theory to physical realizations, *Physical Review B* **101**, 174204 (2020).
- [25] Z.-C. Yang, F. Liu, A. V. Gorshkov, and T. Iadecola, Hilbert-space fragmentation from strict confinement, *Physical Review Letters* **124**, 207602 (2020).
- [26] T. Rakovszky, P. Sala, R. Verresen, M. Knap, and F. Pollmann, Statistical localization: From strong fragmentation to strong edge modes, *Physical Review B* **101**, 125126 (2020).
- [27] S. Moudgalya, A. Prem, R. Nandkishore, N. Regnault, and B. A. Bernevig, Thermalization and its absence within Krylov subspaces of a constrained Hamiltonian, in *Memorial Volume for Shoucheng Zhang* (World Scientific, 2021) pp. 147–209.
- [28] S. Moudgalya, B. A. Bernevig, and N. Regnault, Quantum many-body scars and Hilbert space fragmentation: a review of exact results, *Reports on Progress in Physics* **85**, 086501 (2022).
- [29] S. Moudgalya and O. I. Motrunich, Hilbert space fragmentation and commutant algebras, *Physical Review X* **12**, 011050 (2022).
- [30] R. J. Valencia-Tortora, N. Pancotti, M. Fleischhauer, H. Bernien, and J. Marino, A Rydberg platform for non-ergodic chiral quantum dynamics, arXiv preprint arXiv:2309.12392 (2023).
- [31] S. Scherg, T. Kohlert, P. Sala, F. Pollmann, B. Hebbe Madhusudhana, I. Bloch, and M. Aidelsburger, Observing non-ergodicity due to kinetic constraints in tilted Fermi-Hubbard chains, *Nature Communications* **12**, 4490 (2021).
- [32] T. Kohlert, S. Scherg, P. Sala, F. Pollmann, B. H. Madhusudhana, I. Bloch, and M. Aidelsburger, Exploring the regime of fragmentation in strongly tilted Fermi-Hubbard chains, *Physical Review Letters* **130**, 010201 (2023).
- [33] K. Kim, F. Yang, K. Mølmer, and J. Ahn, Realization of an extremely anisotropic Heisenberg magnet in Rydberg atom arrays, *Physical Review X* **14**, 011025 (2024).
- [34] C. Batista and G. Ortiz, Quantum phase diagram of the  $t - J_z$  chain model, *Physical Review Letters* **85**, 4755 (2000).
- [35] S. Moudgalya, B. A. Bernevig, and N. Regnault, Quantum many-body scars in a Landau level on a thin torus, *Physical Review B* **102**, 195150 (2020).
- [36] H. Labuhn, S. Ravets, D. Barredo, L. Béguin, F. Nogrette, T. Lahaye, and A. Browaeys, Single-atom addressing in microtraps for quantum-state engineering using Rydberg atoms, *Physical Review A* **90**, 023415 (2014).
- [37] C. Ates, T. Pohl, T. Pattard, and J. M. Rost, Antiblockade in Rydberg excitation of an ultracold lattice gas, *Physical Review Letters* **98**, 023002 (2007).
- [38] M. Marcuzzi, J. Minář, D. Barredo, S. De Léséleuc, H. Labuhn, T. Lahaye, A. Browaeys, E. Levi, and I. Lesanovsky, Facilitation dynamics and localization phenomena in Rydberg lattice gases with position disorder, *Physical Review Letters* **118**, 063606 (2017).
- [39] Materials and methods are available as supplementary materials.
- [40] L. Zhao, M. D. K. Lee, M. M. Aliyu, and H. Loh, Floquet-tailored Rydberg interactions, *Nature Communications* **14**, 7128 (2023).
- [41] H. Kim, Y. Park, K. Kim, H.-S. Sim, and J. Ahn, Detailed balance of thermalization dynamics in Rydberg-atom quantum simulators, *Physical Review Letters* **120**, 180502 (2018).
- [42] J. Choi, A. L. Shaw, I. S. Madjarov, X. Xie, R. Finkelstein, J. P. Covey, J. S. Cotler, D. K. Mark, H.-Y. Huang, A. Kale, *et al.*, Preparing random states and benchmarking with many-body quantum chaos, *Nature* **613**, 468 (2023).
- [43] X. Feng and B. Skinner, Hilbert space fragmentation produces an effective attraction between fractons, *Physical Review Research* **4**, 013053 (2022).
- [44] C. Chen, F. Burnell, and A. Chandran, How does a locally constrained quantum system localize?, *Physical Review Letters* **121**, 085701 (2018).
- [45] G. De Tomasi, D. Hetterich, P. Sala, and F. Pollmann, Dynamics of strongly interacting systems: From Fock-space fragmentation to many-body localization, *Physical Review B* **100**, 214313 (2019).
- [46] L. Herviou, J. H. Bardarson, and N. Regnault, Many-body localization in a fragmented Hilbert space, *Physical Review B* **103**, 134207 (2021).
- [47] R. Shen and C. H. Lee, Non-Hermitian skin clusters from strong interactions, *Communications Physics* **5**, 238 (2022).
- [48] R. Lewis-Swan, A. Safavi-Naini, J. J. Bollinger, and A. M. Rey, Unifying scrambling, thermalization and entanglement through measurement of fidelity out-of-time-order correlators in the Dicke model, *Nature Communications* **10**, 1581 (2019).
- [49] D. Hahn, P. A. McClarty, and D. J. Luitz, Information dynamics in a model with Hilbert space fragmentation, *SciPost Physics* **11**, 074 (2021).
- [50] Z. Li, S. Colombo, C. Shu, G. Velez, S. Pilatowsky-Cameo, R. Schmied, S. Choi, M. Lukin, E. Pedrozo-Peñafiel, and V. Vuletić, Improving metrology with quantum scrambling, *Science* **380**, 1381 (2023).
- [51] W. Tian, W. J. Wee, A. Qu, B. J. M. Lim, P. R. Datla, V. P. W. Koh, and H. Loh, Parallel assembly of arbitrary defect-free atom arrays with a multitweezer algorithm, *Physical Review Applied* **19**, 034048 (2023).
- [52] J. R. Johansson, P. D. Nation, and F. Nori, Qutip: An open-source python framework for the dynamics of open quantum systems, *Computer Physics Communications* **183**, 1760 (2012).

## SUPPLEMENTARY INFORMATION

### I. EXPERIMENT SEQUENCE

We first prepare a two-dimensional array [51] of 57–75 static tweezer traps by sending 808 nm light through a pair of acousto-optic deflectors (AODs) and focusing the output beams to a waist of  $0.98(2) \mu\text{m}$  through a microscope objective of numerical aperture  $\text{NA} = 0.5$ . Through light shift measurements, we determine the average trap depth to be 1.0 mK with 2–5% inhomogeneity (relative standard deviation) across the array. Using  $D_1$   $\Lambda$ -enhanced loading, we load the static array of traps with single  $^{87}\text{Rb}$  atoms with  $\geq 80\%$  loading probability. Single-atom detection is performed by fluorescence imaging using optical molasses beams with 99.39(3)% fidelity. We employ a multitweezer algorithm utilizing an array of 852 nm mobile tweezers to assemble three identical defect-free atom chains. The defect-free success probability is about 80% for each chain. In all of our experiments, these chains are spaced about  $3R_b$  apart such that interactions between the chains are on the scale of kHz and can be considered negligible compared to the Rabi frequency, which is on the scale of MHz.

To reduce the in-trap atomic temperature, we perform two stages of cooling. We first employ  $D_1$   $\Lambda$ -enhanced gray molasses to cool the atoms down to  $37(2) \mu\text{K}$ , followed by a preliminary implementation of Raman sideband cooling in 0.6 mK traps for 8 ms. The final atom temperature is  $19(1) \mu\text{K}$  as determined from comparing the measured release-and-recapture probability against Monte Carlo simulations. After cooling, we initialize the atoms in the ground state  $|g\rangle = |5S_{1/2}, F = 2, m_F = 2\rangle$  with 99% fidelity by optically pumping the atoms in the presence of a quantization magnetic field of 3.7 G. The tweezer traps are subsequently turned off during Rydberg excitation.

Our Rydberg excitation follows a two-photon scheme, where a global pulse consisting of a  $\sigma^+$ -polarized 420 nm beam and a counter-propagating  $\sigma^-$ -polarized 1013 nm beam is sent along the quantization axis to excite the atoms to the Rydberg state. The 420 nm laser is red-detuned from the  $|6P_{3/2}, F = 3, m_F = 3\rangle$  intermediate state by  $\Delta' \approx 2\pi \times 780$  MHz, yielding a combined two-photon Rabi frequency of around  $\Omega = 2\pi \times 1.4$  MHz. The Rydberg beam alignment is kept stabilized by piezoelectric mirrors. The damping time for the ground-Rydberg Rabi oscillations of a single atom is measured to be  $\tau = 27(6) \mu\text{s}$  and is well beyond the time scale of dynamics studied in this work.

For most of the experiments, we excite the atoms to the  $|70S_{1/2}, m_J = 1/2\rangle$  Rydberg state. For the QXQ experiment, the interatomic spacing is set to  $a = 7.46 \mu\text{m}$ , resulting in a measured interaction strength of  $V_0 = 2\pi \times 4.9(1)$  MHz. This spacing is changed to  $3.73 \mu\text{m}$  for the QPXPQ and Krylov-restricted thermalization experiments. For the  $\mathbb{Z}_6$  scarring experiment, we instead couple the atoms to the  $|87S_{1/2}, m_J = 1/2\rangle$  Rydberg state. In this case, we use only one defect-free 19-atom chain (as opposed to three defect-free chains) with  $a = 3.89 \mu\text{m}$  to obtain  $V_2 = 2\pi \times 4.3(1)$  MHz.

We implement single-site addressing with the same 852 nm

laser used for atom rearrangement. The single-site addressing beam is applied alongside a global Rydberg  $\pi$ -pulse for initial state preparation. The dynamics of interest are probed with a second global pulse of varying duration, after which atoms in the ground state are recaptured into 1 mK tweezer traps while an additional  $3 \mu\text{s}$  microwave pulse is applied to ionize the Rydberg atoms. The imaging beams are applied a final time to read out the ground (Rydberg) state as the presence (absence) of an atom. We realize a Rydberg detection fidelity of 97(2)%. Each data point shown in this manuscript is averaged from at least 200 defect-free chain samples.

### II. FLOQUET FREQUENCY MODULATION

In our experiments, we use Floquet frequency modulation (FFM) to generate the two drives necessary to realize  $H_{\text{KRT}}$ . Modulating the detuning of a single drive at frequency  $\omega_d$  as  $\Delta(t) = \Delta_0 \sin \omega_d t$  yields a modified Rabi frequency in a rotating frame:

$$\Omega \xrightarrow{\text{FFM}} \Omega \sum_{m=-\infty}^{\infty} i^m J_m(\alpha) e^{im\omega_d t}, \quad (\text{S1})$$

where  $\alpha = \Delta_0/\omega_d$  is the modulation depth. To realize  $H_{\text{KRT}}$ , we set  $\omega_d = V_{k-1}$  and  $\alpha = 2.4$ , the first zero of  $J_0$ . This ensures that the carrier  $m = 0$  component vanishes, while keeping similar amplitudes  $J_1(\alpha) = 0.52$  and  $J_2(\alpha) = 0.43$  for the components in Eq. (S1) that are detuned at  $V_{k-1}$  and  $2V_{k-1}$ , respectively. Correspondingly, the ratio of Rabi frequencies for the two drives is  $\beta = 1.2$ .

In practice, we implement Floquet frequency modulation by sending a focused 420 nm Rydberg laser (beam waist  $25 \mu\text{m}$ ) through an acousto-optic modulator (AOM) in a double-pass configuration. The AOM is in turn driven by an arbitrary waveform generator to achieve a time-varying frequency  $\Delta(t)$ . We calibrate the modulation by monitoring an optical beat note between the first-order deflected beam with a reference beam and find that the modulation depth deviates from the expected value by a linear scaling factor  $\alpha/\alpha_{\text{actual}} = 1.01$ . In addition, we minimize the residual amplitude modulation by compensating for the AOM frequency-dependent diffraction efficiency and by applying a waveform with an optimal set of amplitudes corresponding to the first four harmonics of the modulation frequency [40].

### III. EFFECTS OF POSITION DISORDER

To achieve facilitation, we detune our drive to match the van der Waals interaction strength. Since this interaction depends strongly on the distance between atoms, the dynamics under facilitation are expected to be highly sensitive to the position disorder of our atoms. In particular, a large enough position disorder may result in Anderson-like localization of the state in product-state space [38].

The specific metric governing whether or not localization occurs is the ratio between the interaction disorder and the



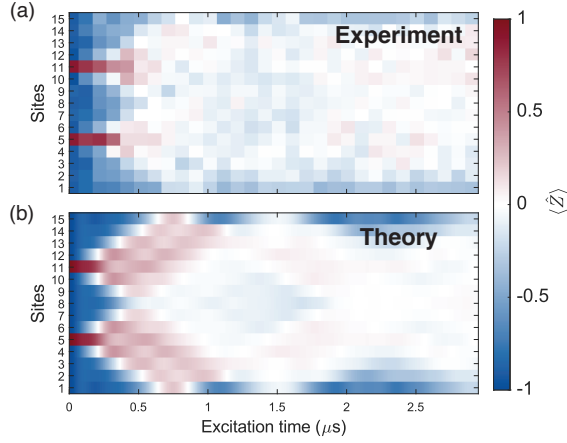


Figure S1. **Dynamics resulting from two initial Rydberg excitations on a 15-atom chain, under the facilitation condition  $\Delta = V_0$ .** (a) The excitations are experimentally observed to spread out, rather than be localized by position disorder, over time. (b) Numerics for the ideal case, assuming no position disorder.

drive strength,  $\sigma_{V_0}/\Omega$ . As reported in Reference [38], localizing behaviour was observed at  $\sigma_{V_0}/\Omega = 1$  and  $\sigma_{V_0}/\Omega = 0.51$ , whereas a ballistic spread of excitations was observed for  $\sigma_{V_0}/\Omega \leq 0.19$ . In our experiment ( $T = 19(1) \mu\text{K}$ , trap depth of 0.6 mK), we estimate the radial atomic position disorder to be  $\sigma_r = 0.087 \mu\text{m}$ . The resultant uncertainty in  $V_{k-1}$  (where  $k = 1$  for the facilitated QXQ model and  $k = 2$  for the QXPQ model) is  $\sigma_{V_{k-1}} = 6|V_{k-1}|\sigma_r/(ka) = 2\pi \times 0.34 \text{ MHz}$ , where  $a$  is the interatomic spacing of our chain. This yields a typical metric of  $\sigma_{V_{k-1}}/\Omega = 0.24$ , which lies near the threshold for ballistic spread of excitations.

Experimentally, we characterize the spread of excitations in our setup to determine if the position disorder of atoms results in a significant localizing effect. We initialize our atom chain with two particular atoms in the Rydberg state, and then measure the site-resolved excitations under the facilitation condition  $\Delta = V_0$  (Fig. S1a). We observe no significant localization of the excitations from position disorder, and the excitation spread dynamics are in reasonable agreement with the ideal theory simulation (Fig. S1b).

#### IV. SYMMETRY BETWEEN QXQ AND PXP

For a 1D chain of equally spaced atoms, the nearest-neighbor approximation to the Rydberg Hamiltonian is given by ( $\hbar = 1$ ):

$$H = -\Delta \sum_{i=1}^N Q_i + \frac{\Omega}{2} \sum_{i=1}^N X_i + \sum_{i=1}^{N-1} V_0 Q_i Q_{i+1} \quad (\text{S2})$$

Setting  $\Delta = 2V_0$  and making the substitution  $Q_i = \mathbb{I} - P_i$ , the Hamiltonian transforms to (neglecting constant energy offsets):

$$H = \frac{\Omega}{2} \sum_{i=1}^N X_i + \sum_{i=1}^{N-1} V_0 P_i P_{i+1} - V_0(Q_1 + Q_N) \quad (\text{S3})$$

The last term is a result of our chain having open boundaries, such that atoms at the ends interact with only one instead of two other atoms. The similar forms of equations (S2) and (S3) reveal the symmetry between the QXQ and PXP models in the bulk.

#### V. EFFECTIVE HAMILTONIANS WITH BEYOND-NEAREST-NEIGHBOR INTERACTIONS

We now consider beyond-nearest-neighbor interactions and derive effective Hamiltonians for our systems in the regime where  $V_0, V_1 \dots V_{k-1} \gg \Omega \gg V_k$ . In other words, we consider the scenario where the first  $k$  orders of interaction are significant to the dynamics at hand ( $k = 1$  corresponds to the nearest-neighbor case). To capture the essential physics, we work with periodic boundary conditions. In this regime, the Hamiltonian is:

$$H = -\Delta \sum_{i=1}^N Q_i + \frac{\Omega}{2} \sum_{i=1}^N X_i + \sum_{j=1}^k \sum_{i=1}^N V_{j-1} Q_i Q_{i+j}. \quad (\text{S4})$$

We then enter the rotating frame with respect to the van der Waals interaction and detuning terms. This corresponds to a unitary transform

$U = e^{it \sum_{j=1}^k \sum_{i=1}^N V_{j-1} Q_i Q_{i+j} - it \Delta \sum_{i=1}^N Q_i}$ . The rotated Hamiltonian is:

$$H' = \frac{\Omega}{2} \sum_{i=1}^N e^{it[-\Delta + \sum_{j=1}^k V_{j-1}(Q_{i+j} + Q_{i-j})]} \sigma_+^i + \text{H.c.}, \quad (\text{S5})$$

where  $\sigma_+^i = |r_i\rangle \langle g_i|$  is the Pauli spin raising operator. Standard commutation relations between Pauli matrices and the Baker-Hausdorff lemma are used to arrive at the equality. Further, using the Pauli identity  $e^{ia\vec{n}\cdot\vec{\sigma}} = \mathbb{I} \cos a + i\vec{n}\cdot\vec{\sigma} \sin a$  and making the substitution  $Q_i = \mathbb{I} - P_i$  where appropriate, we arrive at the expression:

$$H' = \frac{\Omega e^{-i\Delta t}}{2} \sum_{i=1}^N \sigma_+^i \prod_{j=1}^k [(P_{i-j}P_{i+j}) + e^{iV_j-1t} (Q_{i-j}P_{i+j} + P_{i-j}Q_{i+j}) + e^{2iV_j-1t} (Q_{i-j}Q_{i+j})] + \text{H.c.} \quad (\text{S6})$$

In the case of  $k = 1$  (nearest-neighbor interaction only), the above general expression simplifies to:

$$H' = \frac{\Omega e^{-i\Delta t}}{2} \sum_{i=1}^N \sigma_+^i [(P_{i-1}P_{i+1}) + e^{iV_0t} (Q_{i-1}P_{i+1} + P_{i-1}Q_{i+1}) + e^{2iV_0t} (Q_{i-1}Q_{i+1})] + \text{H.c.} \quad (\text{S7})$$

For the remainder of this section (equations (S8)–(S11)), we apply a rotating-wave approximation while ignoring far off-resonant terms. This is valid in the case where  $V_0, \dots, V_{k-1} \gg \Omega$ . For  $k = 1$ , we get the PXP model under  $\Delta = 0$ :

$$H_{\text{PXP}} = \frac{\Omega}{2} \sum_{i=1}^N P_{i-1} X_i P_{i+1}, \quad (\text{S8})$$

whereas setting  $\Delta = 2V_0$  gives us the QXQ model:

$$H_{\text{QXQ}} = \frac{\Omega}{2} \sum_{i=1}^N Q_{i-1} X_i Q_{i+1}. \quad (\text{S9})$$

In the general case of  $k \geq 2$ , setting  $\Delta = 2V_{k-1}$  yields the generalized QPXPQ model as referenced in the main text:

$$H_{\text{QPXPQ}}(k) = \frac{\Omega}{2} \sum_{i=1}^N Q_{i-k} X_i Q_{i+k} \prod_{j=1}^{k-1} P_{i-j} P_{i+j}. \quad (\text{S10})$$

Starting from a state with  $\mathbb{Z}_{2k}$  ordering, under this Hamiltonian, we would then expect only the atoms in the same  $\mathbb{Z}_k$  sector to undergo dynamics, while the rest of the atoms should remain frozen in the ground state. In this constrained Hilbert space, the model may be mapped to a QXQ model on a smaller  $m$ -atom chain, which explains the scarring behavior that is observed. For our experiments with an  $N$ -atom open chain (Figs. 2c, d),  $m = (N + k - 1)/k$ .

From Eq. (S6), our motivation for adding a second drive detuned at  $\Delta = V_{k-1}$  becomes clear: this drive is resonant for atoms that are blockaded by exactly one Rydberg atom  $k$  sites away. Added to the original drive detuned at  $\Delta = 2V_{k-1}$ , this second drive loosens the kinetic constraints exactly  $k$  sites away from the atom, while still maintaining blockade restrictions less than  $k$  sites away. The effective Hamiltonian becomes:

$$H_{\text{KRT}}(k) = \frac{\Omega}{2} \sum_{i=1}^N (Q_{i-k}Q_{i+k} + \beta Q_{i-k}P_{i+k} + \beta P_{i-k}Q_{i+k}) X_i \prod_{j=1}^{k-1} P_{i-j} P_{i+j} \quad (\text{S11})$$

where  $\beta$  is the ratio between the Rabi frequencies of each drive, i.e.  $\beta = \Omega_{V_{k-1}}/\Omega$ . In the main text, we assume  $k = 2$  wherever the argument  $k$  is not explicitly included.

## VI. HILBERT SPACE FRAGMENTATION UNDER $H_{\text{QPXPQ}}$

In this section, we discuss the QPXPQ model and its unusual nonergodic dynamics, which we identify as a consequence of extensive fragmentation of the Hilbert space into many disconnected subspaces. Referencing previous works [23], we briefly examine the resulting frozen states and the spatially disconnected regions separated by these frozen components.

There are exponentially many product states in the local  $Z$ -basis that are invariant under the time evolution operator, referred to as frozen states. The simplest case is the polarized state  $|0\rangle \equiv |\cdots ggggg \cdots\rangle$ , remaining frozen due to the  $Q$  projectors never being satisfied. Similarly,  $|R\rangle \equiv |\cdots rrrrr \cdots\rangle$  remains frozen due to the  $P$  projectors.

---

Based on the ordering of projectors, a list of frozen substrings consisting of five spins can be constructed:  $|\cdots rgggg \cdots\rangle$ ,  $|\cdots ggggr \cdots\rangle$ ,  $|\cdots rggrg \cdots\rangle$ ,  $|\cdots grggr \cdots\rangle$ ,  $|\cdots grrrg \cdots\rangle$ ,  $|\cdots rrrgr \cdots\rangle$ ,  $|\cdots rggrr \cdots\rangle$ . By adding frozen substrings on top of the polarized state, another frozen state is obtained. From the construction we deduce that the quantity of these states grows exponentially with the size of the system. We have demonstrated that substrings of certain patterns remain invariant under the action of  $H_{\text{QPXPQ}}$ . If we now consider a region between two such frozen substrings, this region stays disconnected from the rest of the chain. One can then cover the entire chain with many such regions of varying sizes and locations, surrounded by any such frozen substrings. Each of these regions has its own independent dynamics, giving rise to a large number of disconnected

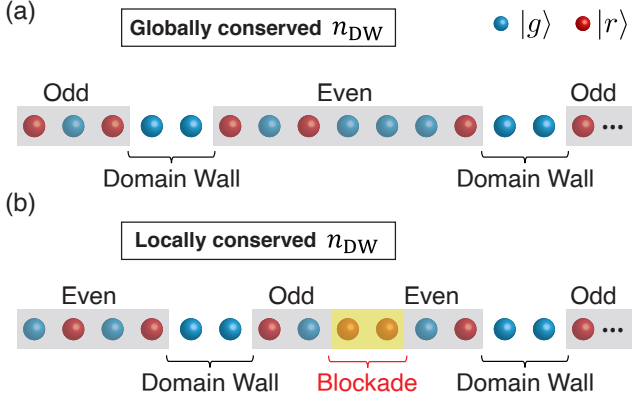


Figure S2. **Domain walls under  $H_{KRT}$ .** (a) Within the primary  $V_0$  block, one can partition the chain into subchains of alternating parity. The number of domain walls  $n_{DW}$  between partitions is globally conserved.  $n_{DW}$ , along with the parity of the leftmost subchain, uniquely identifies a subspace. (b) Outside the primary  $V_0$  block,  $n_{DW}$  is no longer globally conserved, but is instead locally conserved for each sector of the chain separated by  $|rr\rangle$  blocks.

subspaces.

## VII. HILBERT SPACE FRAGMENTATION UNDER $H_{KRT}$

Central to our observation of Krylov-restricted thermalization is the Hilbert space fragmentation exhibited under  $H_{KRT}$ . Fragmented systems cannot be characterized by conventional symmetries [27–29]. Hence, a natural question to ask is the following: is the system truly fragmented, or are there in fact conventional symmetries that uniquely identify each Krylov subspace?

To address this question, we first confine ourselves to the primary  $V_0$  block. We observe that every  $Z$ -basis product state comprises subchains separated by domain walls, which we identify as clusters of even-numbered ground-state atoms (Fig. S2a). Adjacent subchains have alternating parity, which denote whether Rydberg atoms reside on only odd or even sites of the entire chain. (In the main text, the “odd” or “even” subspace refers to the subspace of product states with no domain walls.)

Since spin-flip processes are allowed only when the nearest Rydberg atom is two sites away, we heuristically see that the number of these domain walls,  $n_{DW}$ , remains conserved under  $H_{KRT}$ . This observation prompts us to construct an operator that counts these domain walls, given by the following expression for periodic boundaries:

$$n_{DW} = \frac{n_p}{2} + \frac{1}{2} \sum_{i=1}^s \left[ |Q_{2i-1}P_{2i} - P_{2i}Q_{2i+1}| + |Q_{2i}P_{2i+1} - P_{2i-1}Q_{2i}| \right], \quad (\text{S12})$$

where  $n_p = 0$  and  $s = N/2$  for  $N$  even and  $n_p = Q_N P_1 - P_N Q_1$  and  $s = (N-1)/2$  for  $N$  odd. Intuitively, one of the four terms in the square brackets of Eq. (S12) yields a contribution equal to unity whenever one encounters or leaves a domain wall. On the other hand, for any subchain with Rydberg atoms on only the odd (even) sites, the first and second (third and fourth) terms contribute equally and cancel each other out. Thus, for a given  $n_{DW}$ , the subspace splits into exactly two, each characterized by the parity of the leftmost subchain.

At this point, we have seemingly characterized the subspaces with a global quantum number, which would have implied that the model is not fragmented! However, the above description fails when considering states outside the primary  $V_0$  block. The presence of  $|rr\rangle$  blocks prevents any entanglement from spreading between sections of the chain and  $n_{DW}$  generally fails to uniquely characterize even a finite number of subspaces. The number of domain walls is now only conserved locally for individual sectors of the chain separated by  $|rr\rangle$  blocks (Fig. S2b). Since there are already exponentially many ways to uniquely blockade the chain into subchains [28], the Krylov-restricted thermalization model is indeed fragmented.

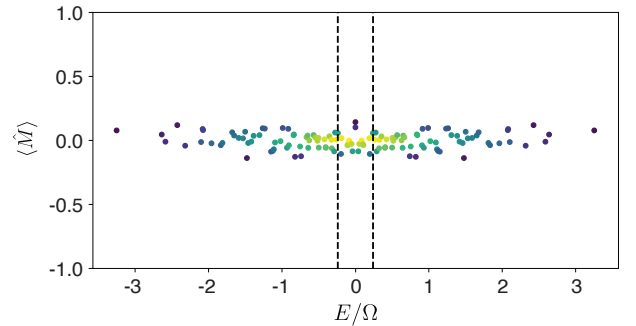


Figure S3. **Distribution of  $\langle \hat{M} \rangle$  for each eigenstate, plotted as a function of the eigenenergy of  $H_{A'}$ .** The two dashed lines mark the energy window  $[-0.24\Omega, 0.24\Omega]$  used to obtain the microcanonical ensemble.

## VIII. PREDICTIONS FROM A MICROCANONICAL ENSEMBLE

To predict the thermal values shown in Figs. 4b and 5, we compute the statistical average of the quantity of interest (e.g.

the staggered magnetization expectation value or the ground state probability) for a microcanonical ensemble. For illustration purposes, we focus on the 13-atom chain thermalizing in

the odd configurational subspace, such that the Hamiltonian for the seven atoms on the odd sites (constituting subarray  $A'$ ) is given by:

$$H_{A'} = \frac{\Omega}{2} (\beta X_1 Q_2 + \beta Q_6 X_7 + \sum_{i=2}^6 (Q_{i-1} Q_{i+1} + \beta Q_{i-1} P_{i+1} + \beta P_{i-1} Q_{i+1}) X_i) \quad (\text{S13})$$

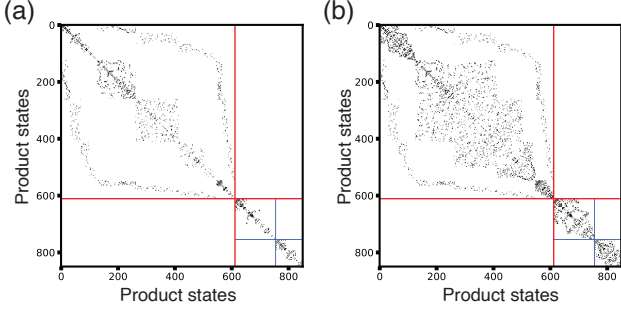


Figure S4. **PPXPP model.** (a) A zoomed-in matrix plot with the boundaries of the first  $V_0$  block marked out. Basis sorting is performed as per Fig. 3. (b) The corresponding matrix when a second drive at  $\Delta = V_1$  is incorporated. We do not see the emergence of any configurational subspaces in the first  $V_0$  block.

where  $\beta = 1.2$  in our experiment. We then average over all the eigenstates of Eq. (S13), projected into the odd configurational subspace, whose energies lie within a narrow window  $[E_0 - \Delta E, E_0 + \Delta E]$  with equal weight. For a system initialized as a product state,  $H_{A'}$  has no diagonal elements, thus the mean energy of the system  $E_0$  is zero. The width of the energy window is chosen to be  $\Delta E = 0.24\Omega$  [9, 11]. In Fig. S3, we show that the staggered magnetization resembles a smooth curve as a function of the eigenenergy. The total number of eigenstates within this energy window is 17, resulting in an averaged value of -0.019, which is plotted in Fig. 4b. Correspondingly, for the odd subspace thermalizing from a different initial state as shown in Fig. 5b, the statistically-averaged ground state probability is 0.53.

For the thermal predictions of the ground state probabilities in the even subspace (Fig. 5a), the total number of eigenstates within the energy window is 9 and the resulting ground state probability is 0.52.

## IX. PPXPP MODEL VERSUS QXPQ MODEL

In the main text, we noted that facilitation is a necessary ingredient to observe the emergence of configurational subspaces in the first  $V_0$  block. To demonstrate this, we consider the converse situation: the blockade-only PPXPP model and its corresponding effective Hamiltonian when a second drive at  $\Delta = V_1$  is added, following the same basis ordering procedure as described in Fig. 3. As expected, after ordering

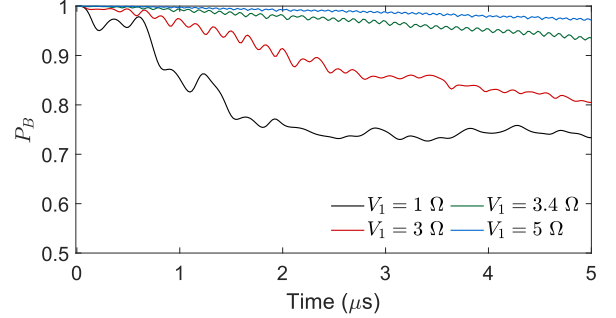


Figure S5. **Effects of deviating from  $H_{\text{KRT}}$ .** Starting from a  $\mathbb{Z}_4$ -ordered state with Rydberg excitations only on subarray  $A$ , atoms in subarray  $B$  remain perfectly frozen in the ground state ( $P_B = 1$ ) if  $H_{\text{KRT}}$  is exactly realized. Off-resonant scattering on our experimental platform results in a PPXPP-type constraint that does not confine time-evolution to the odd or even subspace. Numerics show that smaller values of  $V_1$  result in more serious deviations. Our experimental parameters correspond to  $V_1 = 3.4\Omega$  (green curve), where relatively robust freezing of atoms in subarray  $B$  is observed.

the product states only based on their energies, a block structure emerges corresponding to the  $V_0$  and  $V_1$  energy windows. However, a configuration sort as performed in Fig. 3 does not result in clear disconnected blocks remaining in the first  $V_0$  block after a second drive is added with detuning  $\Delta = V_1$  (Fig. S4a, b), in contrast to the case of  $H_{\text{KRT}}$ . This explains the drop in Fig. S5.

We note that a block structure does emerge in the second  $V_0$  block. In this case, the configurational ordering arises purely from  $|rr\rangle$  sectors that remain frozen, which is a generic feature of both the PPXPP and QXPQ models. On the other hand, states in the second  $V_0$  block can be challenging to access experimentally, so in this work we have focused our efforts on the first  $V_0$  block.

## X. DEVIATIONS FROM EFFECTIVE HAMILTONIANS

Our ability to faithfully realize the effective Hamiltonians  $H_{\text{QXPQ}}, H_{\text{KRT}}$  hinges on the assumption  $V_{k-1} \gg \Omega \gg V_k$ , where  $V_k = V_{k-1}/2^6$  for our equally-spaced atom array. This assumption implies a trade-off between off-resonant scattering to undesired resonances (if  $V_{k-1}$  is not large enough) and residual longer-range interactions (if  $V_k$  is not small enough), both of which give rise to imperfections. In our experiments,

we operate in the range  $V_{k-1}/\Omega = 3.4 \pm 0.1$ . Here we inspect how well imperfections are suppressed under our chosen experimental parameters.

We study the imperfections on  $H_{\text{KRT}}$ , focusing on off-resonant scattering. In  $H_{\text{KRT}}$ , we have two drives detuned at

$$H_{\text{KRT}}^{(1)} = \frac{\Omega}{2} \sum_{i=1}^N P_{i-1} \sigma_+^i P_{i+1} e^{-iV_1 t} [(Q_{i-2} P_{i+2} + P_{i-2} Q_{i+2}) + \beta P_{i-2} P_{i+2} + \beta e^{2iV_1 t} Q_{i-2} Q_{i+2}] + \text{H.c.} \quad (\text{S14})$$

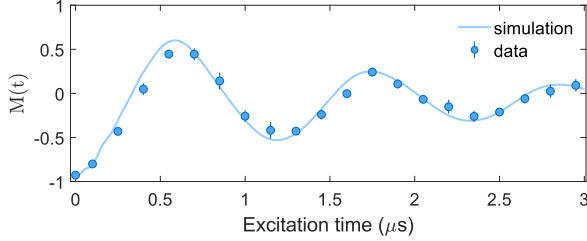


Figure S6. **Dynamics of the PXP  $\mathbb{Z}_2$  scar.** Dependence of the staggered magnetization  $M(t)$  versus time, corresponding to zero detuning.

The first and last terms in the square brackets only lead to a slight adjustment in  $\beta$  and do not fundamentally alter the properties of the Hamiltonian. However, the middle term is a PPXPP-type term that does not, on its own, give rise to configurational subspaces within the first  $V_0$  block. Therefore, we expect that if this term is significant, dynamics from an initial state in the odd (even) subspace will not be confined to the odd (even) subspace. We numerically probe this effect by measuring the ground state density of atoms on the even sites from an initial state in the odd subspace, as  $V_1/\Omega$  is varied. From Fig. S5, we indeed see this leakage effect for smaller values of  $V_1/\Omega$ , where atoms on the odd sites do not remain frozen, whereas the leakage is well suppressed for larger values. Importantly, our numerics show good suppression of this leakage effect for our experimental parameters of  $V_1/\Omega = 3.4$ . Longer-range interactions on our system are small:  $V_2 \approx 0.05\Omega$  and are not expected to be significant.

In  $H_{\text{QPXPQ}}$ , there is only one off-resonant drive, detuned at  $\Delta = 2V_1$ . Thus, the leakage arising from a given finite  $V_1/\Omega$  ratio occurs more slowly compared to that for  $H_{\text{KRT}}$ .

$\Delta_1 = 2V_1$  and  $\Delta_2 = V_1$ . Compared to the ideal  $H_{\text{KRT}}(k=2)$  given by Eq. (S11), there are additional off-resonant terms that would have been neglected from a rotating-wave approximation. To order  $V_1$ , these additional terms are:

## XI. NUMERICAL DETAILS

### A. Simulations

We use the ‘‘Bloqade’’ package in Julia to generate the theory curves in Figs. 2e, 4b, 4d, S1, S5, and S6. For all these curves, we simulate the full Rydberg Hamiltonian (Eq. (1)) and work in the complete Hilbert space of our system.

For Figs. 2e, 4b, and S6, our numerics account for the atom position disorder, Doppler shift, and imperfect state preparation fidelity. An example plot of the staggered magnetization dynamics at zero detuning is given in Fig. S6, which shows reasonable agreement between the experimental data and numerical simulations.

In Fig. 2e, we perform a discrete Fourier transform on the measured staggered magnetization of subarray  $A$ . The intensity of the Fourier transform, denoted as  $|S_A(\omega)|^2$ , is normalized to the frequency domain  $f$  of the single-sided spectrum. The frequency resolution is constrained by the total probe duration, which is  $3 \mu\text{s}$  ( $2.4 \mu\text{s}$ ) for the  $\mathbb{Z}_4$  ( $\mathbb{Z}_6$ ) experiment. The peak is then determined by identifying the maximum normalized intensity within the Fourier transform.

To generate the matrix plots in Figs. 3, 4, and S4, we use the ‘‘QuTiP’’ package [52] to simulate the effective Hamiltonians. To produce Fig. S3, we exactly diagonalize the effective Hamiltonian for a 7-atom open chain and calculate the eigenstates and the expectation values of  $\hat{M}$ .

### B. Definitions of staggered magnetization

In Fig. 4b, we show the staggered magnetization for subarray  $A'$  ( $A$ ) to elucidate the dynamics under  $H_{\text{KRT}}$  ( $H_{\text{QPXPQ}}$ ). The full definitions for the staggered magnetizations are given below:

$$M_{A'}(t) \equiv \frac{1}{N_{A'}} \sum_{i=1}^{N_{A'}} (-1)^i \langle Z_i(t) \rangle, \quad (\text{S15a})$$

$$M_A(t) \equiv \frac{1}{N_A} \sum_{i=2}^{N_{A'}-1} (-1)^i \langle Z_i(t) \rangle, \quad (\text{S15b})$$

where  $i$  indexes the atom on odd sites of the entire chain and  $N_A = N_{A'} - 2$ .